




Why Do Torus-unstable Solar Filaments Experience Failed Eruptions?

Zhenjun Zhou (周振军)^{1,2,3,4} , Xin Cheng^{5,6}, Jie Zhang⁷, Yuming Wang^{3,8}, Dong Wang^{8,9}, Lijuan Liu^{1,3}, Bin Zhuang⁸, and Jun Cui^{1,3}

¹ School of Atmospheric Sciences, Sun Yat-sen University, Zhuhai, Guangdong, 519000, People's Republic of China; zhouzhj7@mail.sysu.edu.cn

² CAS Key Laboratory of Solar Activity, National Astronomical Observatories, Beijing 100012, People's Republic of China

³ CAS Center for Excellence in Comparative Planetology, People's Republic of China

⁴ Southern Marine Science and Engineering Guangdong Laboratory (Zhuhai), People's Republic of China

⁵ School of Astronomy and Space Science, Nanjing University, Nanjing 210093, People's Republic of China; xincheng@nju.edu.cn

⁶ Max Planck Institute for Solar System Research, Göttingen, D-37077, Germany

⁷ Department of Physics and Astronomy, George Mason University, Fairfax, VA 22030, USA

⁸ CAS Key Laboratory of Geospace Environment, Department of Geophysics and Planetary Sciences, University of Science and Technology of China, Hefei, Anhui 230026, People's Republic of China

⁹ Department of Mathematics and Physics, Anhui Jianzhu University, Hefei, Anhui 230601, People's Republic of China

Received 2019 April 24; revised 2019 May 1; accepted 2019 May 15; published 2019 May 30

Abstract

We study the magnetic field and 3D configuration of 16 filament eruptions during 2010 July–2013 February in order to investigate the factors that control the success and/or failure of solar eruptions. All of these events, i.e., eruptions that failed to be ejected and become coronal mass ejections, have filament maximum heights exceeding 100 Mm. The magnetic field of filament source regions is approximated by a potential field extrapolation method. The filament 3D configuration is reconstructed from three vantage points by the observations of *Solar Terrestrial Relations Observatory Ahead/Behind* and *Solar Dynamics Observatory* spacecraft. We calculate the decay index at the apex of these failed filaments and find that in seven cases, their apex decay indexes exceed the theoretical threshold ($n_{\text{crit}} = 1.5$) of the torus instability (TI). We further determine the orientation change or rotation angle of each filament top during the eruption. Finally, the distribution of these events in the parameter space of rotation angle versus decay index is established. Four distinct regimes in the parameter space are empirically identified. We find that all the torus-unstable cases (decay index $n > 1.5$) have large rotation angles ranging from 50° to 130°. The possible mechanisms leading to the rotation and failed eruption are discussed. These results imply that, in addition to the TI, the rotation motion during the eruption may also play a significant role in solar eruptions.

Key words: instabilities – Sun: corona – Sun: coronal mass ejections (CMEs) – Sun: filaments, prominences

Supporting material: animation

1. Introduction

Coronal mass ejections (CMEs) are spectacular bursts of plasma and magnetic field in the Sun's corona. They are frequently associated with solar flares. CMEs and flares are considered to be two observational aspects of the same physical process in a solar eruption (Harrison 1996; Zhang et al. 2001, 2004; Priest & Forbes 2002).

Magnetic flux ropes (MFRs), a set of coiled magnetic field lines winding more than once around a common axis, are believed to be the fundamental structure of CMEs. Coronagraph images of CMEs and in situ measurements of magnetic field validate the fact that the MFR configuration of CMEs exists after the solar eruption (Burlaga et al. 1981; Vourlidas et al. 2013). However, whether an MFR is present in the corona prior to an eruption or is formed during the eruption process is still a subject of debate. Some observational features may contain hints related to the MFRs, including filaments, sigmoids, and hot channels (Kuperus & Raadu 1974; Rust & Kumar 1994; McKenzie & Canfield 2008; Zhang et al. 2012; Cheng et al. 2013). These features may be different manifestations of MFRs, depending on different observational selection effects (e.g., sensitive to different temperatures), perspectives,

as well as magnetic environments (Cheng et al. 2017). Filaments are made of cold and dense plasma suspended in the magnetic dips of an MFR configuration (Guo et al. 2010; Mackay et al. 2010). Filaments are therefore a good tracer of MFRs in the corona (Schmieder et al. 2013; Zhou et al. 2017).

However, MFR eruptions are not always associated with CMEs. For a so-called “failed” filament eruption, a strong deceleration appears in the wake of the initially eruptive-like acceleration. The eruptive filament reaches a maximum height as the mass in the filament threads drains back toward the Sun (Ji et al. 2003), and there is no propagating CME in the white-light coronagraph images. Popular belief attributes such failure to the criteria for the torus instability (TI, in general terms: a sufficiently steep decrease of the overlying field with height) is not met at or above the eruption site (e.g., Török & Kliem 2005; Kliem & Török 2006; Liu 2008; Liu et al. 2012; Song et al. 2014). The critical value is generally suggested to be typically in a range of 1.1–1.5 (e.g., Kliem & Török 2006; Démoulin & Aulanier 2010; Olmedo & Zhang 2010; Zuccarello et al. 2015). Some filament eruptions exhibit a strong rotation motion about its ascending direction and display a characteristic “inverse γ ” shape, which is referred to as the Kink instability (e.g., Hood & Priest 1979; Török & Kliem 2005). However, kink instability is not an effective mechanism for full solar eruptions. It often needs to cooperate with a TI (e.g., Kliem & Török 2006; Liu 2008; Schmieder et al. 2013; Vemareddy & Zhang 2014).



Original content from this work may be used under the terms of the [Creative Commons Attribution 3.0 licence](https://creativecommons.org/licenses/by/3.0/). Any further distribution of this work must maintain attribution to the author(s) and the title of the work, journal citation and DOI.

Table 1
Filament List

| Number | Date YYYY MM DD | Time ^a hhmm | Location | | Flare | h_{\max}^b (Mm) | φ^c ($^\circ$) | n_{\max}^d |
|-----------------|--------------------|---------------------------|----------|----------|-----------|----------------------|-----------------------------|--------------|
| | | | Type | Position | | | | |
| 1 | 2010 Jul 22 | 2307 | QS | N47W22 | * | 126 | 10 | 0.63 |
| 2 | 2011 Jul 24 | 0736 | QS | N61W69 | * | 329 | 2 | 1.02 |
| 3 | 2011 Jul 28 | 0056 | QS | N37E25 | * | 167 | 54 | 0.99 |
| 4 | 2011 Sep 28 | 0207 | QS | N39E09 | * | 147 | 114 | 1.49 |
| 5 | 2011 Nov 04 | 1927 | AR | N44E23 | * | 209 | 83 | 0.69 |
| 6 | 2011 Dec 25 | 1146 | QS | S25W23 | C8.4 | 155 | 86 | 2.80 |
| 7 | 2012 Jan 01 | 0137 | AR | N24W34 | * | 162 | 16 | 1.43 |
| 8 | 2012 Mar 04 | 1745 | AR | N14W40 | C3.3 | 235 | 50 | 1.91 |
| 9 | 2012 May 05 | 1746 | AR | N16E35 | C3.0 | 129 | 130 | 2.20 |
| 10 | 2012 Aug 11 | 1656 | AR | S19E18 | C2.0 | 134 | 103 | 2.87 |
| 11 | 2012 Aug 16 | 1826 | AR | S22W49 | B5.3 | 172 | 99 | 1.64 |
| 12 | 2012 Oct 25 | 0436 | AR | N16W48 | C2.6 | 148 | 67 | 2.25 |
| 13 ^e | 2012 Nov 12 | 0430 | AR | S24W17 | * | 186 | 87 | 1.72 |
| 14 ^e | 2012 Nov 29 | 1220 | AR | N15E58 | C4.5 C5.8 | 136 | 73 | 1.48 |
| 15 | 2013 Feb 04 | 0117 | QS | S52E88 | * | 137 | 3 | 0.92 |
| 16 | 2013 Feb 07 | 0226 | QS | S49W79 | * | 177 | 1 | 0.85 |

Notes.^a Time of filament reaching its maximum height in FOV of *STEREO* EUVI.^b Reconstructed maximum height of the filament.^c Rotation angle during the eruption.^d The corresponding decay index at filament's maximum height position.^e In this table, events with dagger-shaped symbols are observed by AIA at 193 Å and EUVI at 195 Å, the rest are seen at 304 Å by AIA and EUVI.

Recently, an experimental result has demonstrated that torus-driven eruptions can fail under a weak kink onset condition (Myers et al. 2015). Using solar observations, Jing et al. (2018) pointed out that the TI onset criteria is not a necessary condition for CMEs, some TI-stable MFRs can manage to break through the strong “strapping” field and evolve into CMEs. The eruption is additionally influenced by other factors, such as the T_w (twist number in the MFRs; Myers et al. 2015; Liu et al. 2016), $\Delta\varphi$ (the change of orientation of the polarity inversion line (PIL) as a function of height; Baumgartner et al. 2018). Meanwhile, with a strong writhing, the erupting MFR may experience a dissolution by magnetic reconnection with the overlying flux, resulting in a failed eruption (Hassanin & Kliem 2016). Anyway, most of the previous observational studies of failed eruptions could not reveal the exact mechanism associated with it.

Uncovering what prevents an evolving eruption from becoming ejective surely improves our understanding of the requirements for a solar eruption. Using the 3D reconstruction by exploiting observations of multiple views and the potential field source surface (PFSS) model (Schrijver & De Rosa 2003), we have investigated 16 failed filament eruptions. We find out that the writhe of failed filament eruption varies significantly from event to event, and the amount of writhe depends on the decay index of strapping magnetic field. In Section 2, we describe our event sample as well as the data and methods used. The details of the analysis are described in Section 2, and the obtained results and discussions are presented in Section 3.

2. Observation and Analysis

2.1. Instruments

The twin *Solar Terrestrial Relations Observatory* (*STEREO*) A (*Ahead*), B (*Behind*) and *Solar Dynamics Observatory* (*SDO*) provide us with an unprecedented

opportunity to observe filaments in a multiview setting. The Atmospheric Imaging Assembly (AIA; Lemen et al. 2012) on board *SDO* can observe a filament in narrow extreme-UV (EUV) passbands including 304 Å (formation temperature $T_f = 10^5$ K) and 193 Å ($T_f = 1.58 \times 10^6$ K) with a high cadence (12 s), high spatial resolution (0.6'' per pixel), and large field of view (FOV; $1.3R_\odot$). Meanwhile, the Extreme Ultraviolet Imager (EUVI) on board *STEREO* provides another view of the filament at similar wavelengths, i.e., 304 Å ($T_f = 6 \sim 8 \times 10^5$ K) and 195 Å ($T_f = 1.4 \times 10^6$ K) with an FOV of $1.7R_\odot$ (Howard et al. 2008). For a failed filament eruption, evolutions of height and velocity have exactly the same trend as the hot-channel prior to it ceasing to rise (Cheng et al. 2014). Utilizing these multiview observations, we apply 3D reconstruction to obtain the 3D configuration and evolution of filaments of study. The Helioseismic and Magnetic Imager (HMI; Schou et al. 2012), also on board *SDO*, provides photospheric vector magnetic field data with a cadence up to 45 s and a pixel size of 0.5''. We have employed three different coronagraphs, *Solar and Heliospheric Observatory* (*SOHO*)/Large Angle and Spectrometric Coronagraph (LASCO)-C2 (Brueckner et al. 1995) and *STEREO*/Sun Earth Connection Coronal and Heliospheric Investigation (SECCHI)-COR1 A and B (Howard et al. 2008), to determine whether a filament eruption results in CME or not, i.e., a successful eruption or a failed eruption.

2.2. Selection of Events

Sixteen failed filament eruptions are selected in this study (Table 1) according to the following criteria (e.g., Figure 1): (1) It is a failed filament eruption, i.e., no corresponding CME is captured in LASCO/C2 or SECCHI/COR1 (Figure 1(b)). (2) The source region of the filament should be located on the solar disk in the view of *SDO*/AIA to allow for the coronal magnetic field extrapolation, as well as in the limb view of *STEREO*/

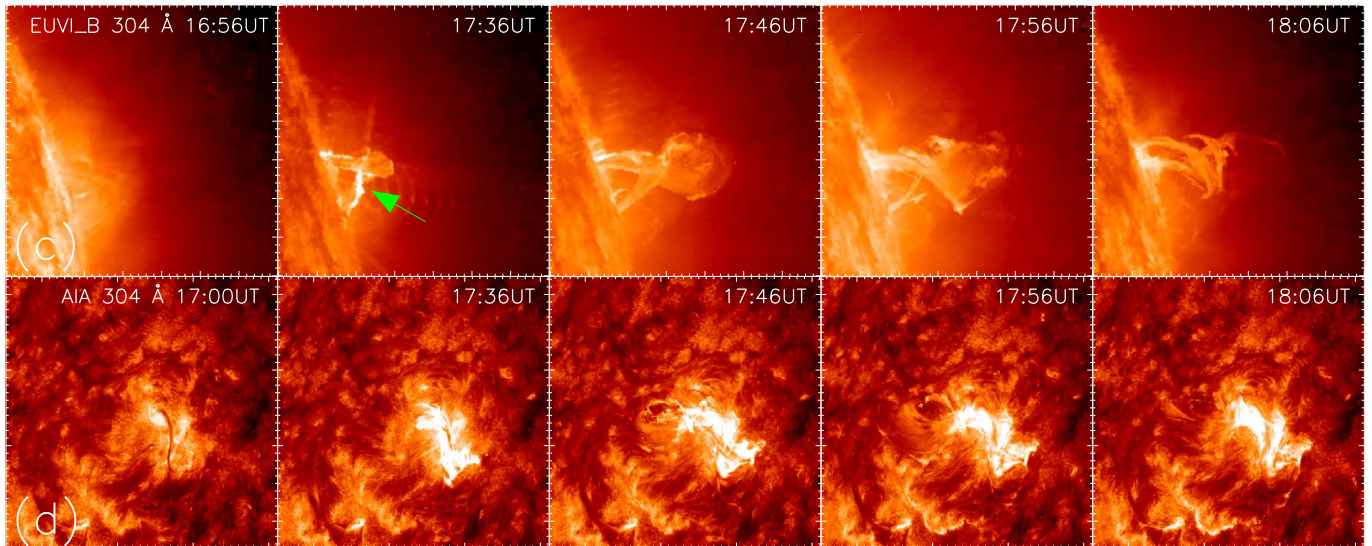
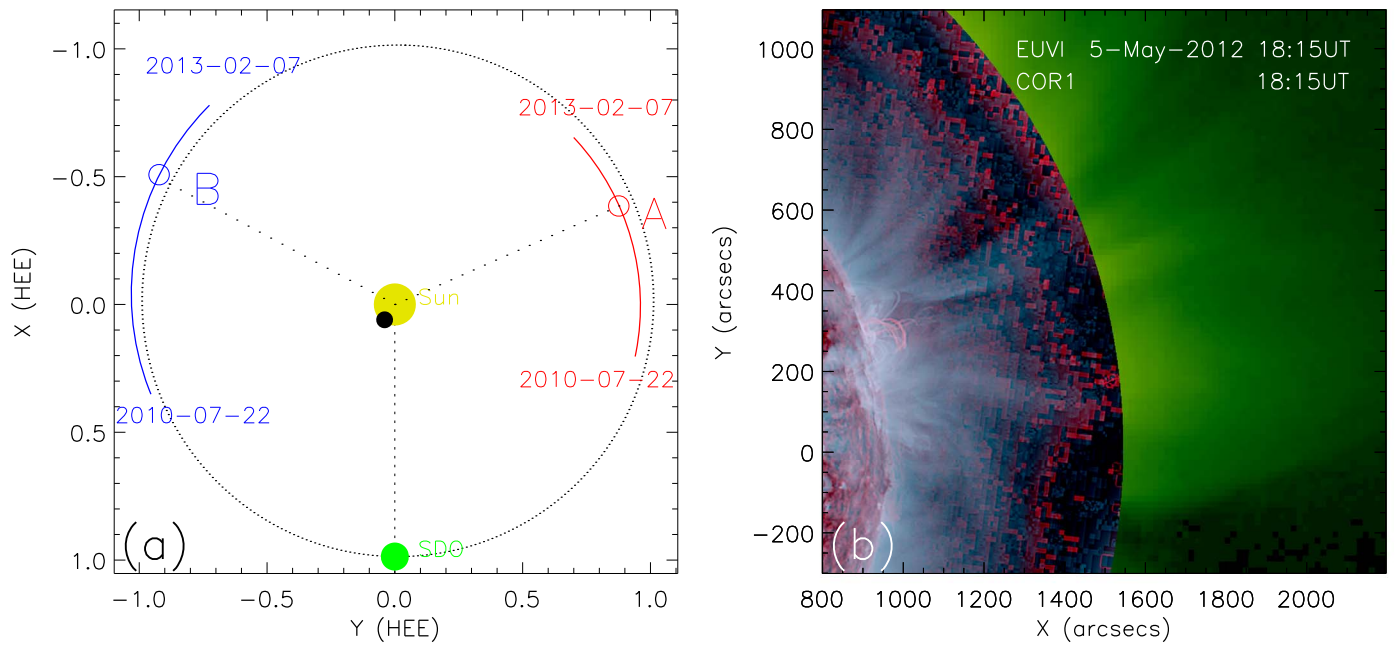


Figure 1. The selection criteria of failed filaments. Panel (a) displays the paths of the *STEREO-A* (red arc) and *B* (blue arc) and position of *SDO* (green dot) in the ecliptic plane during the period from 2010 July 22 to 2013 February 07. The blue and red circles indicate the positions of *STEREO-A/B* on 2012 May 5 when a failed filament eruption occurred. The black dot on the Sun marks the filament source region, which appears on the solar disk when viewed from *SDO*, on the limb from *STEREO-B*, and on the backside of the Sun from *STEREO-A*. Panel (b) shows no obvious CME signal in *STEREO-B* COR1 and EUVI 304 and 195 Å composite image acquired during the filament eruption. Panels (c) and (d) provide observations of the prominence morphology during the eruption from the limb view in *STEREO-A* EUVI 304 Å and the disk view in *SDO/AIA* 304 Å, respectively. An animation of the two views of the eruption process in the 304 Å passband is available online. The animation runs from \sim 17:00 UT to 18:26 UT.

(An animation of this figure is available.)

EUVI as is necessary for 3D reconstructions (e.g., Figures 1(c), (d)). (3) The terminal height of the filament can be exactly determined. In this study, we only consider the cases in which the maximum height exceeds 100 Mm. An erupting filament that stops at a lower altitude is inclined to be torus-stable in its later evolution due to the “relatively high probability” of a small decay index at the lower heights. Since the purpose of this study is to examine the nature of failure of torus-unstable events, the choice of high heights makes our selection of event unambiguous.

Based on these criteria, we examine *SDO/AIA* and *STEREO/EUVI* data to search for suitable filament eruption events from 2010 July to 2013 February, during which the near-quadrature configuration of *STEREO A/B* allows for the best 3D view of a solar eruption (see Figure 1(a)). We have successfully identified 16 such events, which are listed in Table 1. Through browsing the evolution of these 16 filament eruptions, we find out part of these cases show a strong rotation motion, hence we focus on the relationship between the rotation motion and filament eruption.

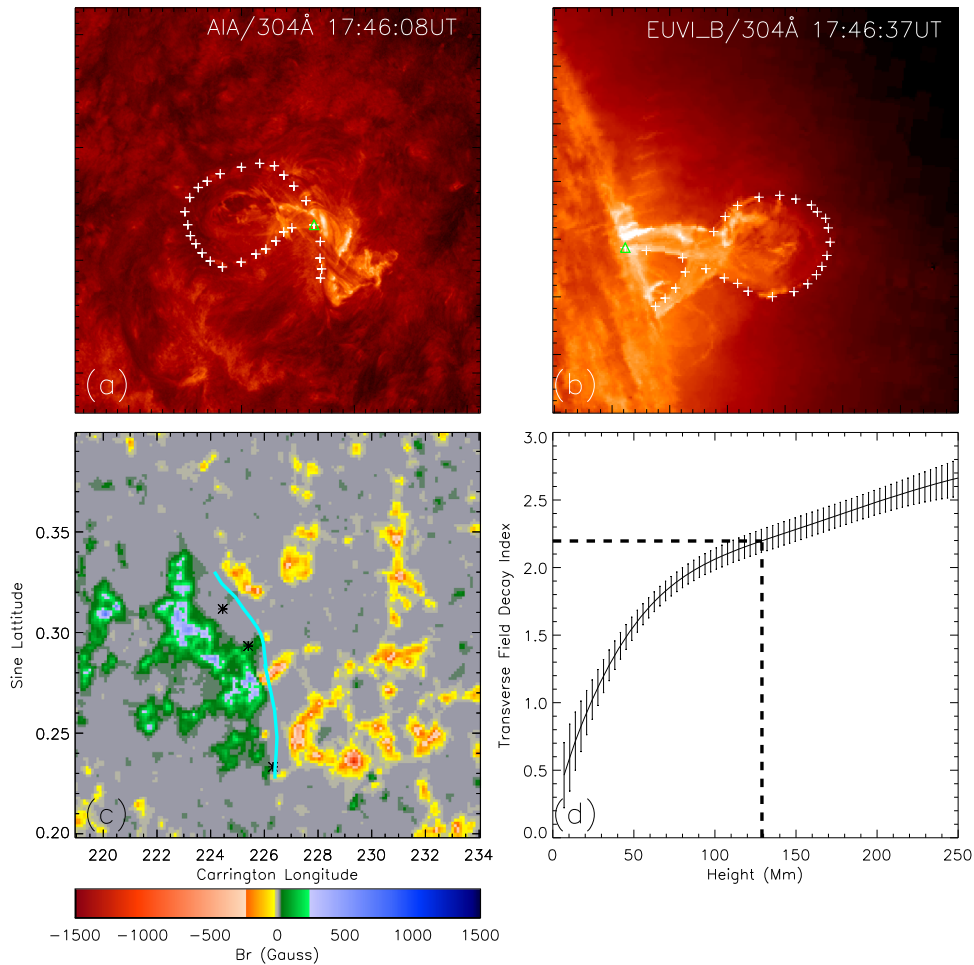


Figure 2. Calculation of the decay index at the maximum height of the failed erupted filament. The white plus symbols in panels (a) and (b) depict the prominence spine. The green triangle symbol denotes the same point viewed in two different angles (from *SDO* and *STEREO-B*). Panel (c) shows the line-of-sight magnetic field in the source region of the filament, and black asterisks mark out the projected location of the filament before the eruption. A cyan line denotes the PIL near this filament. In panel (d), the decay index n as a function of the height h above the surface in units of Mm. The vertical and horizontal lines indicate the maximum height and the corresponding decay index.

2.3. Decay Index and Rotation Angle

For the 16 selected events, we create a parameter space that characterizes the TI and the writhing morphological change. The critical parameter for the TI is the decay index ($n = -d \ln B_{\text{ex}} / d \ln h$, where B_{ex} is the horizontal component of external field perpendicular to the radial component B_r in spherical coordinates). Here we employ the PFSS model to calculate the coronal magnetic field based on the synoptic map of the photospheric radial field. It should be noted that only the transverse component of the extrapolated potential field is used, because the radial component does not contribute to the downward confinement onto the erupting MFRs. The final decay index is an average value along the main PIL. We use the 2012 May 5 event (No. 9 in Table 1) as an example to demonstrate how the decay index at its maximum height is calculated. Figures 2(a) and (b) show the erupted filament stopping at a certain height in *SDO* and *STEREO-B* view angles. We reconstruct the 3D coordinates of several selected points along the erupted filament axis using `scc_measure.pro` routine, which is available in SolarSoftWare (Freeland & Handy 2012). The maximum height of the filament is thus determined to a good degree. We sample the segment of the PIL directly underneath the filament by clicking on the segment

as uniformly as possible to get sufficient representative points (marked by cyan line in Figure 2(c)), and then calculate the decay index n at different heights for each selected point. In Figure 2(d), we plot n as a function of h , which is averaged over all selected points, with the error bar indicating the standard deviation. The filament final decay index corresponding to the maximum height can be found through interpolation of these discrete $n(h)$ nodal values, the uncertainty of the final decay index can also be estimated by interpolation. For this case, we obtain that the decay index at maximum height $n_{\text{max}h} = 2.20 \pm 0.09$. Note that the threshold value of TI is believed to be 1.5 for a toroidal current channel (Kliem & Török 2006). Thus, this derived $n_{\text{max}h}$ is significantly larger than the theoretical critical value. In the meantime, n increases monotonically as the height increases, so there is no local torus-stable confinement (Wang et al. 2017). Obviously, this filament eruption is in the torus-unstable state but failed.

Here, we look into the writhing morphological change during the eruption of these events. The writhe is proportional to the difference in angle between the tangent vector at the top and the line connecting the footpoints (Török et al. 2010). To evaluate the writhe during the eruption, we calculate the rotation angle φ from the reconstructed filament. The same case is employed as the example. We project the erupted filament

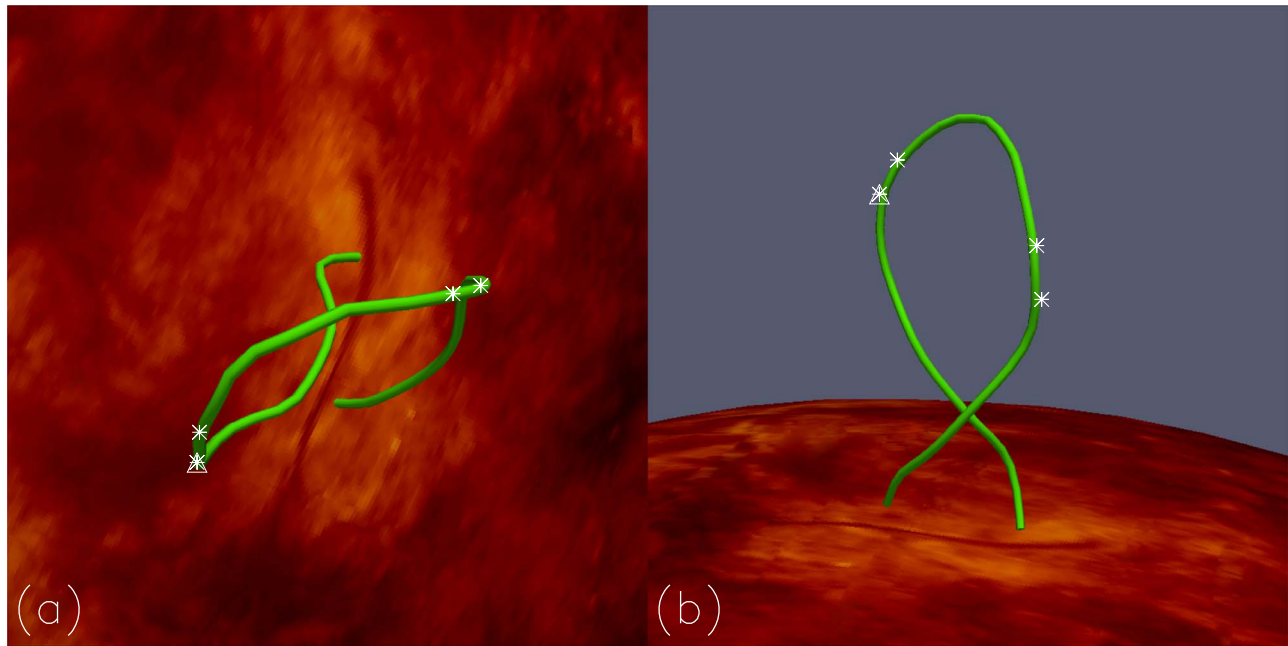


Figure 3. Calculation of rotation angle during the eruption. The reconstructed 3D filament (colored in green) during the eruption from the top view (a) and side view (b), the bottom boundaries are the projected AIA 304 Å synoptic map. Asterisks point to the shoulder of the filament.

onto the solar disk from the top view (See Figure 3(a)). Here we use the line connecting the elbows as the proxy of the tangent vector at the top. Four points (white asterisks in Figures 3(a)–(b)) selected near the two elbows are used for fitting. The projected filament top is represented by a fitted regression line. φ is then given as the difference in angle between the fitted regression line and the line connecting the footpoints. The image sequence (Figure 1(d)) also shows that the rotation is clockwise (CW; viewed from above) for this filament eruption. For this case, we calculated the rotation angle and its corresponding error ($\varphi = 130^\circ \pm 1^\circ.6$). Its error originates from the uncertainty of the elbow’s location.

3. Results and Discussion

Figure 4 shows the scatter diagram of TI parameters n versus rotation angle φ (with estimated uncertainties) for the 16 failed filament eruptions. The failed events with decay index n less than 1.5 (9 out of 16 cases) may be consistent with the present understanding of the TI. In the TI model, an erupting filament cannot evolve into a CME when its decay index has not achieved the theoretical expectation ($n \geq n_{\text{crit}} = 1.5$) (Kliem & Török 2006). However, exceptions to this theory do exist. The decay indexes of the other seven cases (red color events in Figure 4) exceed more than 1.5, but they do not result into CMEs. This result argues against this conception that the TI is a sufficient condition for a full eruption. Here we call these exceptions torus-unstable failed eruptions. Interestingly, all these torus-unstable events show a strong rotation during the eruptions. Their rotation angles (φ) exceed 40° with an average value of 89° . The critical rotation angle, $\varphi \sim 40^\circ$, discriminates best between those torus-stable and torus-unstable failed filament eruptions. There is not a single case located in the region of the large decay index ($n \geq 1.5$) and small rotation angle ($\varphi \leq 40^\circ$) regime. Thus four distinct regimes can be empirically identified in the parameter space as shown in Figure 4.

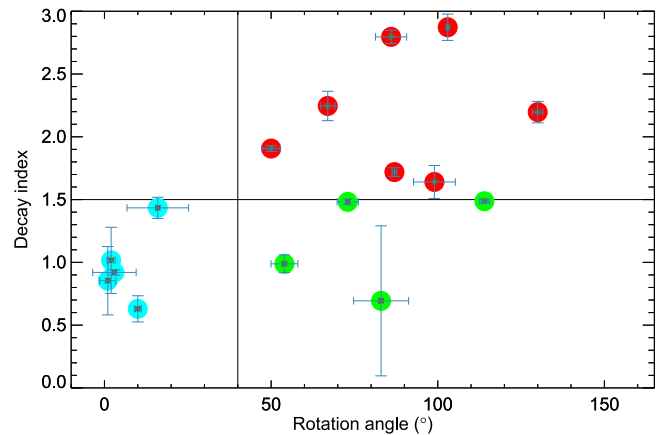


Figure 4. Scatter diagram of rotation angle vs. decay index at the maximum heights for 16 failed filament eruptions. The vertical and horizontal black lines, which are empirically identified, delineate the four distinct instability parameter regimes described in the text. Cases in the same regime are the same color.

Apparently, the rotation motion of a filament has a certain correlation with the failed eruption. Previous models concerning the writhing of MFRs have opposite effects for an eruption: On one hand, the writhing of the MFR’s upper part into the orientation of the overlying arcade is energetically favorable for passing through the overlying arcade to become a CME (Sturrock et al. 2001; Fan 2005). On the other hand, the helical deformation facilitates interchange reconnection between filament flux and ambient flux (Hassanin & Kliem 2016) and/or reconnection between the legs of the rope (Alexander et al. 2006; Liu & Alexander 2009; Kliem et al. 2010), such reconnection progressively decrease the flux content of the rope, up to its full destruction. This interaction is signified by the brightenings and nonthermal sources near the body or the crossing point of the filament (Karlický & Kliem 2010; Cheng et al. 2018). When only considering the torus-unstable failed eruptions, the reconnection caused by the MFR writhing seems

dominant, an intense brightening in the body of the filament supports this possibility (see the brightening pointed by green arrow in 17:36 UT of Figure 1(c)). The simulation of Török et al. (2010) pointed out that confined MFR eruptions tend to show stronger writhe at low heights than ejective eruptions (CMEs). Hassanin & Kliem (2016) further inferred that if an eruption is halted, then the magnetic tension of the erupting flux can no longer be relaxed by expansion but only by further writhing, resulting in a tendency for confined eruptions to develop a strong writhing.

In summary, 16 failed filament eruptions are studied with both the AIA on board the *SDO* and EUVI on board *STEREO*. Their decay indexes are obtained from the PFSS model and rotation angle are calculated with the help of the 3D reconstruction. Thus we establish the scatter diagram of TI parameters n versus rotation angle φ . Seven cases are theoretically in the torus-unstable state. Meanwhile, they all show strong writhing motions during the eruptions with rotation angle $\geq 40^\circ$. It seems that writhing and failed eruption show a complex coupling relationship. The possible reconnection due to the filament rotational motion may ruin the architecture of the MFR, resulting in a failed eruption. Simultaneously, this confinement induces a strong rotation instead of a further expansion. More detailed observational analysis, theoretical considerations, and numerical simulations are necessary toward a comprehensive understanding of the MFR eruption.

We acknowledge the SECCHI, AIA, and HMI consortia for providing excellent observations. Z.J. is supported by the Open Research Program of CAS Key Laboratory of Solar Activity (KLSA201811). X.C. is funded by NSFC grants 11722325, 11733003, 11790303, and 11790300, Jiangsu NSF grants BK20170011, and the Alexander von Humboldt foundation. J. Z. is supported by US NSF AGS-1249270 and NSF AGS-1156120. D.W. acknowledges support by Natural Science Foundation of Anhui Province Education Department (KJ2017A493, gxyq2018030). Y.W. is supported by NSFC grants 41574165, 41761134088, and 41774178. L.L. is supported by the Open Project of CAS Key Laboratory of Geospace Environment, and NSFC grants 11803096. J.C. is supported by NSFC grants 41525015 and 41774186. Z.J. appreciates discussions with and support of Prof. G.P.Zhou, Dr. C.Xia, and Dr. Y.Guo.

Software: SolarSoftWare (Freeland & Handy 2012), ParaView (Ahrens et al. 2005; Ayachit 2015).

ORCID iDs

Zhenjun Zhou

(周振军)  <https://orcid.org/0000-0001-7276-3208>

References

- Ahrens, J., Geveci, B., & Law, C. 2005, in *The Visualization Handbook*, ed. C. D. Hansen & C. R. Johnson (Cambridge, MA: Academic Press), 717
- Alexander, D., Liu, R., & Gilbert, H. R. 2006, *ApJ*, **653**, 719
- Ayachit, U. 2015, *The ParaView Guide: A Parallel Visualization Application* (Clifton Park, NY: Kitware)
- Baumgartner, C., Thalmann, J. K., & Veronig, A. M. 2018, *ApJ*, **853**, 105
- Breckner, G. E., Howard, R. A., Koomen, M. J., et al. 1995, *SoPh*, **162**, 357
- Burlaga, L., Sittler, E., Mariani, F., & Schwenn, R. 1981, *JGR*, **86**, 6673
- Cheng, X., Zhang, J., Ding, M. D., Liu, Y., & Poomvises, W. 2013, *ApJ*, **763**, 43
- Cheng, X., Ding, M. D., Zhang, J., et al. 2014, *ApJL*, **789**, L35
- Cheng, X., Guo, Y., & Ding, M. 2017, *SoChE*, **60**, 1383
- Cheng, X., Kliem, B., & Ding, M. D. 2018, *ApJ*, **856**, 48
- Démoulin, P., & Aulanier, G. 2010, *ApJ*, **718**, 1388
- Fan, Y. 2005, *ApJ*, **630**, 543
- Freeland, S. L., & Handy, B. N. 2012, *SolarSoft: Programming and data analysis environment for solar physics*, Astrophysics Source Code Library, ascl:1208.013
- Guo, Y., Schmieder, B., Démoulin, P., et al. 2010, *ApJ*, **714**, 343
- Harrison, R. A. 1996, *SoPh*, **166**, 441
- Hassanin, A., & Kliem, B. 2016, *ApJ*, **832**, 106
- Hood, A. W., & Priest, E. R. 1979, *SoPh*, **64**, 303
- Howard, R. A., Moses, J. D., Vourlidas, A., et al. 2008, *SSRv*, **136**, 67
- Ji, H., Wang, H., Schmahl, E. J., Moon, Y.-J., & Jiang, Y. 2003, *ApJL*, **595**, L135
- Jing, J., Liu, C., Lee, J., et al. 2018, *ApJ*, **864**, 138
- Karlický, M., & Kliem, B. 2010, *SoPh*, **266**, 71
- Kliem, B., Linton, M. G., Török, T., & Karlický, M. 2010, *SoPh*, **266**, 91
- Kliem, B., & Török, T. 2006, *PhRvL*, **96**, 255002
- Kuperus, M., & Raadu, M. A. 1974, *A&A*, **31**, 189
- Lemen, J. R., Title, A. M., Akin, D. J., et al. 2012, *SoPh*, **275**, 17
- Liu, R., & Alexander, D. 2009, *ApJ*, **697**, 999
- Liu, K., Wang, Y., Shen, C., & Wang, S. 2012, *ApJ*, **744**, 168
- Liu, R., Kliem, B., Titov, V. S., et al. 2016, *ApJ*, **818**, 148
- Liu, Y. 2008, *ApJL*, **679**, L151
- Mackay, D. H., Karpen, J. T., Ballester, J. L., Schmieder, B., & Aulanier, G. 2010, *SSRv*, **151**, 333
- McKenzie, D. E., & Canfield, R. C. 2008, *A&A*, **481**, L65
- Myers, C. E., Yamada, M., Ji, H., et al. 2015, *Natur*, **528**, 526
- Olmedo, O., & Zhang, J. 2010, *ApJ*, **718**, 433
- Priest, E. R., & Forbes, T. G. 2002, *A&ARv*, **10**, 313
- Rust, D. M., & Kumar, A. 1994, *SoPh*, **155**, 69
- Schou, J., Scherrer, P. H., Bush, R. I., et al. 2012, *SoPh*, **275**, 229
- Schmieder, B., Démoulin, P., & Aulanier, G. 2013, *AdSpR*, **51**, 1967
- Schrijver, C. J., & De Rosa, M. L. 2003, *SoPh*, **212**, 165
- Song, H. Q., Zhang, J., Cheng, X., et al. 2014, *ApJ*, **784**, 48
- Sturrock, P. A., Weber, M., Wheatland, M. S., & Wolfson, R. 2001, *ApJ*, **548**, 492
- Török, T., Berger, M. A., & Kliem, B. 2010, *A&A*, **516**, A49
- Török, T., & Kliem, B. 2005, *ApJL*, **630**, L97
- Vemareddy, P., & Zhang, J. 2014, *ApJ*, **797**, 80
- Vourlidas, A., Lynch, B. J., Howard, R. A., & Li, Y. 2013, *SoPh*, **284**, 179
- Wang, D., Liu, R., Wang, Y., et al. 2017, *ApJL*, **843**, L9
- Zhang, J., Cheng, X., & Ding, M.-D. 2012, *NatCo*, **3**, 747
- Zhang, J., Dere, K. P., Howard, R. A., Kundu, M. R., & White, S. M. 2001, *ApJ*, **559**, 452
- Zhang, J., Dere, K. P., Howard, R. A., & Vourlidas, A. 2004, *ApJ*, **604**, 420
- Zhou, Z., Zhang, J., Wang, Y., Liu, R., & Chintzoglou, G. 2017, *ApJ*, **851**, 133
- Zuccarello, F. P., Aulanier, G., & Gilchrist, S. A. 2015, *ApJ*, **814**, 126